

Accepted to ApJ (July 1, 2013)

Direct Imaging of a Compact Molecular Outflow from a Very Low-luminosity Object; L1521F-IRS

Satoko Takahashi

*Joint ALMA Observatory, Alonso de Cordova 3108, Vitacura, Santiago, Chile;
National Astronomical Observatory of Japan, 2-21-1 Osawa, Mitaka, Tokyo 181-8588,
Japan;
Academia Sinica Institute of Astronomy and Astrophysics, P.O. Box 23-141, Taipei 10617,
Taiwan
satoko.takahashi@nao.ac.jp*

Nagayoshi Ohashi

*Subaru Telescope, National Astronomical Observatory of Japan, North Aohoku Place Hilo
HI 96720, USA
Academia Sinica Institute of Astronomy and Astrophysics, P.O. Box 23-141, Taipei 10617,
Taiwan*

Tyler L. Bourke

*Harvard-Smithsonian Center for Astrophysics, 60 Garden Street Cambridge, MA 02138, U.
S. A.*

ABSTRACT

Studying the physical conditions of very low-luminosity objects (VeLLOs; $L_{\text{bol}} < 0.1 L_{\odot}$) is important for understanding the earliest evolutionary stage of protostars and brown dwarfs. We report interferometric observations of the VeLLO L1521F-IRS, in ^{12}CO (2–1) line emission and the 1.3 mm continuum emission, using the Submillimeter Array (SMA). With the ^{12}CO (2–1) high-resolution observations, we have spatially resolved a compact but poorly collimated molecular outflow associated with L1521F-IRS for the first time. The blueshifted and redshifted lobes are aligned along the east and west side of L1521F-IRS with a lobe size of ≈ 1000 AU. The estimated outflow mass, maximum outflow velocity, and outflow force are $(9.0\text{--}80)\times 10^{-4} M_{\odot}$, 7.2 km s^{-1} , and

$(7.4-66)\times 10^{-7} M_{\odot} \text{ km s}^{-1} \text{ yr}^{-1}$, respectively. The estimated outflow parameters such as size, mass, and momentum rate are similar to values derived for other VeLLOs, and are located at the lower end of values compared to previously studied outflows associated with low- to high-mass star forming regions. Low-velocity less collimated ($1.5 \text{ km s}^{-1}/1200 \text{ AU}$) and higher-velocity compact ($4.0 \text{ km s}^{-1}/920 \text{ AU}$) outflow components are suggested by the data. These velocity structures are not consistent with those expected in the jet driven or wind driven outflow models, perhaps suggesting a remnant outflow from the FHSC as well as an undeveloped outflow from the protostar. Detection of an infrared source and compact millimeter continuum emission suggest the presence of the protostar, while its low bolometric luminosity ($0.034-0.07 L_{\odot}$), and small outflow, suggests that L1521F is in the earliest protostellar stage ($< 10^4 \text{ yr}$) and contains a substellar mass object. The bolometric (or internal) luminosity of L1521F-IRS suggests that the current mass accretion rate is an order-of-magnitude lower than expected in the standard mass accretion model ($\approx 10^{-6} M_{\odot} \text{ yr}^{-1}$), which may imply that L1521F-IRS is currently in a low activity phase.

Subject headings: ISM: clouds — ISM: individual objects (L1521F-IRS, Taurus) — stars: jet and outflow — stars: protostars — ISM: molecules — stars: formation — stars: low-mass

1. INTRODUCTION

Studying the earliest phase of star formation is an important issue for understanding the initial conditions of star formation. Previous studies of star formation have focused on dense cores associated with class I/0 protostars, whereas these class I/0 objects are rather well-developed protostars with estimated ages of 10^4-10^5 yr . According to the conventional accretion scenario of protostars (e.g., Stahler et al. 1980), in which the accretion luminosity is given as $GM_*\dot{M}_{\text{acc}}/R_*$ (G is the gravitational constant, \dot{M}_{acc} is the mass accretion rate, and M_* and R_* are the mass and the radius of the protostar, respectively), extremely young protostars in a very early phase of the accretion process are less luminous when compared with well-developed protostars. Such extremely young protostars, though their total number would be small because of their short time scale, have most probably not been identified in many previous studies. In order for us to study the initial conditions, or extremely early phase of star formation, it is crucial for us to pay more attention to starless cores, where no bright infrared sources are found. Starless cores with high central densities ($\geq 10^5 \text{ cm}^{-3}$) are sometimes called pre-stellar cores, as they show signs of evolution toward the formation of a

protostar, such as inward motions (e.g., L1544; Tafalla et al 1998. Ohashi et al. 1999).

Great progress in the study of starless cores has been made using the *Spitzer* Space Telescope, which archived unprecedented sensitivity ($L < 1 L_{\odot}$) in nearby star-forming regions. Spitzer observations have identified a large number of low-luminosity candidates, including 15 Very Low Luminosity Objects, or VeLLOs ($L_{\text{bol}} < 0.1L_{\odot}$; Di Francesco et al. 2007, Bourke et al. 2005, 2006; Dunham et al. 2008; Terebey et al. 2009). The first VeLLO, L1014-IRS, was discovered at the center of a “starless” core with a bolometric luminosity of $0.09 L_{\odot}$ (Young et al. 2004). Follow up SMA observations toward VeLLOs, L1014-IRS and L1451-mm, have detected outflows associated with them. The estimated outflow parameters suggest that VeLLOs have the most compact, the lowest mass and the least energetic outflows compared with known Class 0/I outflows (Bourke et al. 2006; Pineda et al. 2011). These results suggest that L1014-IRS would be a very low-mass protostar (i.e., proto-brown dwarf star) and L1451-mm is a candidate of First Hydro-Static Core (FHSC). Recent detailed case studies of VeLLOs or similar targets present some variety in their nature such as the mass of parental core, outflow parameters, and outflow morphology (Bourke et al. 2005; 2006; Terebey et al. 2009; Belloche et al. 2002; 2006; Chen et al. 2010; Dunham et al. 2010; Pineda et al. 2011; Kauffmann 2011; Dunham et al. 2011). However, the nature of VeLLOs are not clear yet due to their limited in number.

There are three possible scenarios for the nature of VeLLOs. Some source are proto-brown dwarfs, extremely young protostars, or young stellar objects, which are in a low-state of accretion phase (not necessarily “extremely young”). Studying these candidates is very important because for sources related to the first type are crucial to investigate the formation and evolution of brown dwarfs. Sources of the second type are related to the earliest stage of star formation, and provide a missing link between low-mass star formation at a very earlier evolutionary phase, finding a missing link between the prestellar phase and the Class 0 phase. Theories predict that the earliest protostellar phase is the important FHSC phase, followed by the subsequent formation of a protostar (Larson 1969; Masunaga & Inutsuka 2000; Bate 1998, 2010; Saigo et al. 2008; Schonke & Tscharnuter 2011). Studies of VeLLOs are crucial to observationally test the protostar formation scenario through FHSC. Sources of the third type are crucial to understand how the accretion process terminate at the last phase of the young stellar evolution or how the accretion can be periodic.

In order to study nature of VeLLOs, in this paper we focus on a detailed case study of the VeLLO, L1521F-IRS, which is located in the Taurus molecular cloud ($d = 140$ pc; $L_{\text{IR}} = 0.024 L_{\odot}$). The parental core, L1521F (or MC 27 by Mizuno et al. 1994), was originally noticed as a starless condensation with a high-central density of $\approx 10^6 \text{ cm}^{-3}$ (Onishi et al. 1998), and lately identified as the second example of a VeLLO (Bourke et al. 2006). Molecular

depletion observed in CCS and the enhanced deuterium fraction imply that L1521F is at the time one of the two best examples of an evolved starless core in the Taurus molecular cloud ($d = 140$ pc), along with L1544 (Crapsi et al. 2004; 2005; Shinnaga et al. 2004). In contrast to another VeLLO core, L1014, L1521F was identified as the most evolved starless core, may be suggesting that they are extremely young protostars. Asymmetric spectra observed in HCO^+ (4–3 and 3–2) emission, suggest infalling gas motions with a size scale of 2000–3000 AU (Onishi et al. 1999). The *Spitzer* observations discovered a reflection nebula and a point source associated with L1521F (Bourke et al. 2006). The estimated luminosity is 0.034–0.07 L_{\odot} (Bourke et al. 2006; Terebey et al. 2009). Detection of a 100 AU scale dust continuum source with 1.3 mm PdBI observations (Maury et al. 2010) supports the claim that the protostar has already formed at the center of L1521F. Recent single-dish studies in the CO (7–6 and 6–5) emission detected warm (~ 30 –70 K) and extended (~ 2400 AU) gas, suggesting that these emission may be originated from shock gas at the interface between the outflow and dense core (Shinnaga et al. 2009).

In this paper, we present the 1.3 mm dust continuum and ^{12}CO (2–1) results obtained from the Submillimeter Array (SMA; Ho et al. 2004). Goals of the paper are to (i) search for a compact molecular outflow associated with L1521F-IRS, (ii) investigate the physical properties of the molecular outflow, (iii) compare its properties with molecular outflows detected from other candidate VeLLOs, and (iv) discuss the evolutionary stage of L1521F-IRS.

The SMA observations and data reduction are explained in Section 2. The synthesized SMA images, derived physical parameters, spectra and kinematics of CO (2–1) emission and the 1.3 mm continuum emission are presented in Section 3. Outflow properties, evolutionary phase, and the origin of L1521F-IRS are discussed in Section 4. Finally Section 5 summarizes the project.

2. OBSERVATIONS AND DATA REDUCTION

The ^{12}CO (2–1; 230.538 GHz), ^{13}CO (2–1; 220.39868 GHz), C^{18}O (2–1; 219.56036 GHz), N_2D^+ (3–2; 231.321 GHz) and 1.3 mm continuum observations were carried out with the eight 6 m antennas of the SMA¹ in its compact configuration on January 3, 2007. The phase center was set at R.A.(J2000) = $4^{\text{h}}28^{\text{m}}38.95^{\text{s}}$, decl.(J2000) = $26^{\circ}51'35''.1$. Zenith opacities at

¹The Submillimeter Array is a joint project between the Smithsonian Astrophysical Observatory and the Academia Sinica Institute of Astronomy and Astrophysics and is funded by the Smithsonian Institution and the Academia Sinica.

225 GHz were typically in the range between 0.18–0.2. The typical system noise temperature in DSB mode was between 100–200 K. Both the LSB and USB data were obtained simultaneously by the digital spectral correlator, which has a bandwidth of 2 GHz in each sideband. The SMA correlator was configured with high spectral resolution windows of 256 channels over 104 MHz for ^{12}CO (2–1) and ^{13}CO (2–1), and 1024 channels over 104 MHz for C^{18}O (2–1) and N_2D^+ (3–2). These provide channel spacing of 0.53 km s^{-1} and 0.13 km s^{-1} , respectively. After subtracting the spectral windows where CO (2–1), ^{13}CO (2–1), and C^{18}O (2–1) are located at, the LSB and USB continuum data, separated by 10 GHz, were combined to improve the sensitivity. The effective bandwidth for the continuum emission is approximately 3.0 GHz.

The phase and amplitude were calibrated by observations of 3C 111 (3.0 Jy), while the passband calibration was made through observations of the quasar 3C 279. The flux calibration was performed by observations of Uranus. The overall flux uncertainty was estimated to be $\sim 20\%$. The array provided projected baselines ranging from 9 to 53 k λ , so that our observations were insensitive to structure larger than $18''$ (equivalent to 2500 AU) at the 10 % level (Wilner & Welch 1994), but have good sensitivity to spatial scales below this. The primary FWHM beam of the SMA is $\sim 55''$ at this frequency.

The raw data were calibrated using MIR, originally developed for the Owens Valley Radio Observatory (OVRO; Scoville et al. 1993) and adopted for the SMA. After the calibration, final CLEANed images were made with the AIPS task IMAGER. In order to image the extended faint continuum emission, Natural weighting with a Gaussian taper (FWHM=30 k λ , corresponding to $6''$) was used for the 1.3 mm continuum data, while natural weight with no taper was used for the strongly detected ^{12}CO (2–1) data. The resultant angular resolutions of the images are $4''.8 \times 4''.4$ and $3''.1 \times 2''.7$ for the 1.3 mm continuum and ^{12}CO (2–1) data, respectively. The achieved rms noise levels of the 1.3 mm continuum and ^{12}CO (2–1) images are $1.3 \text{ mJy beam}^{-1}$, and $0.13 \text{ Jy beam}^{-1}$ in a 0.53 km s^{-1} channel, respectively. Note that the ^{13}CO (2–1) line was barely detected ($\leq 5\sigma$), so the data were only used for the opacity estimation described in Section 3.3.2. No C^{18}O (2–1) nor N_2D^+ (3–2) emission was detected even after smoothing the channels. The observational parameters for CO (2–1) and 1.3 mm continuum are summarized in Table 1.

3. RESULTS

3.1. 1.3 mm Continuum Emission

Figure 1 shows the 1.3 mm continuum emission toward L1521-IRS detected with the SMA (white contours), superposed on the 1.2 mm continuum emission obtained with the IRAM 30 m/MAMBO-2 (black contours and grey scale). We have detected the 1.3 mm continuum emission with a peak position of R.A.(J2000) = $4^h28^m38.82^s$, decl.(J2000)= $26^\circ51'34''.1$. The total flux density and peak intensity are measured to be 11 mJy and 6.8 ± 1.3 mJy beam $^{-1}$, respectively. The position and peak flux were derived with the AIPS task “imstat”, while the total flux was derived from two dimensional Gaussian fitting with the AIPS task “imfit”. The peak position of 1.3 mm continuum is roughly consistent with previous single-dish results in the (sub)millimeter continuum emission (Shinnaga et al 2004; Crapsi et al. 2004; Kauffmann et al. 2008). The structure of the 1.3 mm continuum emission is elongated in the east-west direction with a deconvolved size of $5''.0$ (700 AU), while the structure along the north-south direction is not spatially resolved with our SMA observations.

On the assumption that the dust emission is optically thin at 1.3 mm and the temperature distribution of the dust-continuum emission is uniform, the mass of the dust condensation is estimated to be $0.047 - 0.084 M_\odot$, and the lower limit of molecular hydrogen column density is estimated to be $(1.3 - 2.3) \times 10^{23}$ cm $^{-22}$. For the derivation, we assumed that $\beta=1.5-2.0$, a dust temperature of 10 K (e.g., Myers & Benson 1983), a gas-to-dust ratio of 100, and $\kappa_0 = 0.0899$ cm 2 g $^{-2}$ at 1.3 mm (Ossenkopf & Henning 1994). When a dust temperature of 30 K instead of 10 K is adopted, the estimated mass becomes larger by a factor of 5. The flux density of the 1.3 mm continuum emission measured with the SMA corresponds to 7.6 % of the flux density measured within the $10''.5$ beam of the IRAM/MAMBO-2 1.2 mm observations, which is 90 mJy (Crapsi et al. 2004).

Although the SMA 1.3 mm continuum emission is associated with the Spitzer source, its peak position is shifted by $2''.0$ from the mean position of the Spitzer continuum bands in which infrared source is detected (wavelength longer than the $5.8 \mu\text{m}$ band; Bourke et al. 2006). Since near infrared emission in the *Spitzer*/IRAC image may be attributed mainly to scattered light, we have also checked the position of the $24 \mu\text{m}$ source taken with the *Spitzer*/MIPS; it is found that the peak position of $24 \mu\text{m}$ emission is much closer to the mean position of *Spitzer*/IRAC image than the SMA 1.3 mm continuum source position. Since

²The upper size of the continuum source, which is 700×620 AU, was derived from the deconvolved size of the major axis and the beam size of the minor axis using the 2D Gaussian fitting tool AIPS “imfit”, and then, the mean number density was estimated with the assumption of an elliptical shaped structure

the positional shift between the 1.3 mm and infrared sources is approximately 9 times larger than the positional accuracy of the SMA observations, $0''.23$, the positional shift between the 1.3 mm continuum source and the infrared source is significant. Here, the positional accuracy of the SMA observations was derived from combination of the signal-to-noise ratio (S/N) of source and the beam size relation: $\sigma_{\text{SN}} \approx (1/2\pi)(\theta/(S/N)) \approx 0''.19$, and baseline error of the SMA observations: $\sigma_{\text{BL}} \approx 0.1\lambda \approx 0''.13$; which is $\approx \sqrt{\sigma_{\text{SN}}^2 + \sigma_{\text{BL}}^2} \approx 0''.23$.

Observations of L1521F using the Plateau de Bure Interferometer (PdBI) at a angular resolution of $0''.49 \times 0''.27$ by Maury et al. (2010) in 1.3 mm continuum emission detected a compact source associated with the Spitzer source. The reported peak flux of 1 mJy beam^{-1} (8.3σ detection) by PdBI is much weaker than the peak flux of the continuum emission detected by SMA, and the deconvolved size of $0.65''$ ($\sim 90 \text{ AU}$) is much more compact than the SMA continuum emission. The origins of these continuum sources detected with the SMA and PdBI are discussed in Section 4.1.

3.2. First Detection of Compact Molecular Outflow associated with L1521F-IRS

The ^{12}CO (2–1) emission was detected at blueshifted ($V_{\text{LSR}} = 2.9\text{--}6.1 \text{ km s}^{-1}$) and redshifted ($V_{\text{LSR}} = 8.2\text{--}10.3 \text{ km s}^{-1}$) velocities in our SMA observations. Figure 2 shows integrated intensity maps of the blueshifted and redshifted emission, superposed on the $4.5 \mu\text{m}$ image obtained with the *Spitzer*/IRAC. This is the first time that the CO outflow emission associated with L1521F-IRS has been spatially resolved and their distributions are directly compared with the reflection nebula obtained with *Spitzer*/IRAC. The CO emission extends approximately $18''$ (2500 AU) with the signal-to-noise level of more than three. The near infrared reflection nebula as well as the high-extinction region around L1521F-IRS shown in Figure 2a suggest that the axis of the outflow cavity is aligned at a position angle of 75° (denoted as dashed line in Figure 2a). The detected CO emission is elongated almost in the east-west direction, which is similar to the near-infrared nebula. Careful inspection reveals that the infrared nebula is slightly brighter to the west of L1521F-IRS, suggesting that the western part of the reflection nebula is slightly tilted to the near-side from the plane of the sky (i.e., envelope inclination angle of $50^\circ\text{--}70^\circ$; Terebey et al. 2009). Furthermore, the reflection nebula indicates a wide opening angle cavity, hence it is expected that both blue and redshifted CO emission appears in both outflow lobes. The observed CO (2–1) emission shows more complicated structures than the reflection nebula. The blueshifted CO emission is brighter on the eastern side, which is in the opposite sense to what might be expected from the reflection nebula image. This may be a consequence of the non-uniform distribution of

the surrounding material. The absence of the redshifted emission can be explained by the absorption from foreground diffuse gas, as mentioned in Section 3.3. The CO integrated emission shows a parabolic shaped structure, especially in the blueshifted velocity detected in the eastern part of the emission (Figure 2a and 2b).

Further, as presented in Figure 2c, compact CO blue and redshifted components located to the north-east of L1521F-IRS are distributed symmetrically with respect to a point denoted by an open star. This might suggest that the SMA CO emission traces multiple outflows from a binary system (one associated with L1521F-IRS and another one associated with a new source, L1521F-NE). However, no driving source has been detected in either millimeter continuum emission with PdBI/SMA or infrared emission with *Spitzer* the open star position (L 1521F-NE), with a mass detection limit of $0.0005 M_{\odot}$ ³ (Maury et al. 2010; This work). Since there is no strong evidence to support the 2nd case, in this paper, we consider that a single outflow is driven by L1521F-IRS, and discuss the velocity structures and physical parameters as the single outflow.

Figure 3 shows velocity-channel maps of ^{12}CO (2–1) emission, with a velocity interval of 0.53 km s^{-1} . Here, we adopt the systemic velocity of 6.5 km s^{-1} obtained from the single-dish N_2D^+ spectrum measured by Crapsi et al. (2004). In the velocity-channel maps no blueshifted or redshifted components with velocity more than $|V_{\text{LSR}} - V_{\text{sys}}| > 4.5 \text{ km s}^{-1}$ were detected at a 3σ level. The blueshifted component in the velocity range of $V_{\text{LSR}}=4.0\text{--}4.5 \text{ km s}^{-1}$ is located at $2''$ west of the protostar position (i.e., position of *Spitzer* point source as well as the PdBI 1.3 mm source). In the velocity range of $V_{\text{LSR}}=5.1\text{--}6.1 \text{ km s}^{-1}$, three emission peaks surrounding the protostar are detected. No significant emission ($> 3\sigma$) was detected close to the systemic velocity of $V_{\text{LSR}}=6.6\text{--}7.7 \text{ km s}^{-1}$. This is most likely due to the lack of sensitivity to large-scale structures, mainly originated from extended emission such as an ambient envelope, although, as will be discussed in Section 3.3, missing flux originated from the outflow is less likely significant. In addition, self-absorption of the CO emission would also responsible for the less significant emission at $V_{\text{LSR}}=6.6\text{--}7.7 \text{ km s}^{-1}$ (see more detail in Section 3.3). The redshifted components in the velocity range of $V_{\text{LSR}}=8.2\text{--}8.8 \text{ km s}^{-1}$ are detected to the north-east and west of the protostar position. The most redshifted components in the velocity range of the $9.3\text{--}10.3 \text{ km s}^{-1}$ are detected $9''$ west of the protostar position.

The CO emission is elongated in an east-west direction, which is consistent with the extension of the near-infrared nebula observed in the *Spitzer*/IRAC image. Hence, it is likely

³The mass detection limit are derived from the $3\times\text{rms}$ noise level obtained with the PdBI observations by Maury et al. (2010) with assumptions of $\beta=1.5$ and $T=20\text{K}$ (refer more detail in Section 3.1)

that the CO emission trace the outflow. In fact, the observed mean CO velocity, $\approx 2 \text{ km s}^{-1}$, is significantly larger than the velocity required to escape from the typical stellar mass in Taurus ($0.8 M_{\odot}$; Luhman et al. 2009 at 1000 AU, which is $\approx 0.7 \text{ km s}^{-1}$). Moreover, if the CO emission is associated with the near-infrared nebula, the intrinsic CO velocity should be larger than the observed CO velocity. Considering with the inclination angle of between 20° and 40° (Terebey et al. 2009; pole-on is defined as an outflow inclination angle of 0°), velocities larger by factors of 2.9 and 1.6 would be expected. This argument suggests that the CO emission is most likely gravitationally unbound. Recent PdBI observations by Maury et al. (2010) did not detect the high velocity CO (2–1) components. This suggests that the high velocity CO is relatively extended, but not compact enough to be detected with the PdBI observations weighted toward the long baseline lengths.

3.3. CO Spectra

In order to discuss the outflow properties, we focus on the compact CO outflow components detected with the SMA. The nature of any extended outflow component is unclear and requires combining the SMA data with single-dish data to recover extended missing flux. A full analysis of these data are beyond the scope of this paper, and we note that no high-velocity and extended outflow emission has been reported previously. In this paper, we investigate the missing flux using SMA CO (2–1) spectra compared with recently observed single-dish CO (2–1) spectra using the Submillimeter Telescope (SMT; Ohashi et al. in prep.).

Figure 4 presents a comparison of the SMA and SMT CO spectra at the phase center. For the spectral comparison, the SMA CO data have been convolved with a SMT $32''$ beam, and both the SMA and SMT spectra are compared in units of brightness temperature. Figure 4a compares the CO (2–1) spectra between the SMT and SMA. In order to compare the high-velocity CO component originated from the outflow, a “residual” spectrum was derived from the difference between the SMT spectrum at the protostar position and a mean spectrum of the spectra at $30''$ offsets from the central position (Figure 4b thin line). Here, we assume that the CO (2–1) emission originating from the molecular outflow is dominant within $R < 2000 \text{ AU}$ ($< 14''$). This assumption is probably reasonable because no large-scale molecular outflow has been reported from any previous single-dish studies. Further, the detection of higher transition CO (7–6 and 6–5) emission, which may originate in the shocked gas between the outflow and dense envelope gas, also shows a similar size (Shinnaga et al. 2009). With this reasoning, the emission at positions offset from the protostar mostly comes from emission in the protostellar envelope. Subtraction of the mean spectrum of

the offset positions from the central spectrum is presented in Figure 4b as thin line. The residual spectrum shows a high-velocity component likely originating from the molecular outflow associated with L1521F-IRS. The residual CO emission appears in the LSR velocity range of 4.4 to 6.5 km s⁻¹ and 8.0 to 9.4 km s⁻¹. Comparison between the SMA spectrum and the SMT residual spectrum is presented in Figure 4b. Both spectra show a similar spectral shape with roughly the same velocity ranges. This simple analysis suggests that missing flux in the high-velocity compact component is not significant in the SMA data.

In the SMT CO (2–1) spectrum, two intensity peaks were detected with the LSR velocity at 5.9 km s⁻¹ and 7.5 km s⁻¹. These velocity peaks are shifted from the cloud systemic velocities, $V_{\text{sys}} = 6.5 \text{ km s}^{-1}$. The CO spectrum taken with the SMT is poorly fitted by a single-Gaussian component centered at the systemic velocity of L 1521F cloud, $v_{\text{sys}} = 6.5 \text{ km s}^{-1}$. One possibility to explain this is the presence of a secondary component located along the same line of sight with a different systemic velocities. The line profile with a peak velocity of 7.5 km s⁻¹ is only detected in the lower transitions of CO (1–0 and 2–1; Our SMT data presented in Figure 4a) and ¹³CO (1–0) (Takakuwa et al. 2011; Ohashi et al. in prep.), which have low-critical densities of $n_c \sim 10^2 \text{ cm}^{-3}$, but not in other dense gas tracers such as H¹³CO⁺, N₂H⁺, and N₂D⁺ (Onishi et al. 1999; Crapsi et al. 2006; Shinnaga et al. 2004). If the secondary component (diffuse cloud) is located in the foreground of the L1521F main cloud, and if the temperature of the second cloud is colder than the L1521F main cloud, it is possible that CO emission from the L 1521F system is absorbed by the CO emission of the second cloud. Note that this idea also explains the missing redshifted emission seen in the SMA CO (2–1) spectrum with a velocity range of 6.5 to 8.2 km s⁻¹ (Figure 4 thick line), as well as the sharp decrease in emission in the redshifted velocity component observed in the position-velocity (P-V) diagram presented in Figure 5 (will be discussed in Section 3.4). This sharp emission decrease is likely due to the self-absorption rather than missing flux in the SMA observations. If the lack of emission is due to the missing short baselines, we should see the missing flux symmetrically centered at the systematic velocity (6.5 km s⁻¹).

3.4. Velocity Structure

Previous outflow studies favor two different models for the origin of outflows (e.g., Lee et al. 2000). One is **the wind-driven model**: molecular outflows consist of swept-up gas entrained by a wide-angle outflow. The other is **the jet-driven model**: molecular outflows consist of ambient gas swept up by the bow shock at the jet head. These two models show different spatial distributions as well as different kinematic features in a position-velocity (P-V) diagram cut along the outflow axis. The wind-driven model shows a parabolic structure

in the P-V diagram that originates from the central star, while the jet-driven model produces a large-velocity dispersion ($>$ several 10 km s^{-1}) at the jet head (e.g., Lee et al. 2000).

A position-velocity (P-V) diagram of the ^{12}CO (2–1) emission cut along the axis of the molecular outflow (P.A.= 75° passing through the *Spitzer*/IRAC position) is shown in Figure 5. Here, we compare the observed CO outflow with simple analytical outflow models discussed in Lee et al. (2000). In the cylindrical coordinate system, the structure and velocity of a parabolic shaped shell can be described as follows;

$$z = CR^2, \quad v_R = v_0R, \quad v_z = v_0Z \quad (1)$$

where z is the distance along the outflow axis, R is the radial size of the outflow perpendicular to z , C and v_0 are free parameters that describe the spatial and velocity distributions of the outflow shell, respectively.

Note that redshifted emission with the LSR velocity range between 6.5 to 8.0 km s^{-1} was missed due to the foreground absorption, so that in the velocity analysis, we mainly focus on the blueshifted emission. The outflow shell was delineated following the blueshifted component of the CO intensity map obtained with the SMA and the *Spitzer* $4.5 \mu\text{m}$ image in order to determine the free parameter C (Figure 2a and 2b). Adopting the outflow inclination angle of 30° (the median value estimated from Terebey et al. 2009), the curvatures of the parabolic shell surface, C , was derived as $0.022 \text{ arcsec}^{-1}$. With the values of C and i fixed, the model P-V diagram was compared with the observational results by varying the free parameter v_0 . As an example, the solid line in Figure 5 is produced by $i = 30^\circ$, $C=0.022 \text{ arcsec}^{-1}$, $v_0 = 0.05 \text{ km s}^{-1}$. Varying v_0 can change the curvature of the PV model, presented in the solid line in Figure 5. If we assume that the velocity structure follows these simple models, a wind-driven outflow model predicts the Hubble law velocity structure, that is the velocity increases as the emission moves away from the central stars. The observed outflow velocity structure toward L1521F does not agree with the Hubble-law type velocity structure, which delineate parabolic shape in PV diagram, as denoted in Figure 5. The L1521F outflow also does not show the large-velocity dispersion at the jet head, which is expected in the jet-driven outflow. These results suggest that the velocity structure of the L1521F outflow does not follow those observed in the low-mass protostellar outflow/jets in the Class 0 phase (e.g., Lee et al. 2000, 2007a, b, Hirano et al. 2010).

In addition to the low-velocity extended components, a higher velocity component has also been detected around the position of L1521F-IRS. The blueshifted emission of this component extends up to the velocity of $|V_{\text{LSR}} - V_{\text{sys}}| = 3.6 \text{ km s}^{-1}$. The velocity channel maps (Figure 3) also show the high velocity blueshifted component concentrated at the

L1521F-IRS with the LSR velocity of 2.9 to 6.1 km s⁻¹. Assuming that the inclination angle of the outflow is $\sim 30^\circ$, the intrinsic maximum velocity can be ~ 7.2 km s⁻¹. As we discussed in Section 3.2, this emission is gravitationally unbound (even assuming the most massive stellar mass in Taurus), and hence, unlikely tracing infalling or rotational motion of the envelope gas.

A gravitationally unbound compact CO component has been observed toward a Class 0 source, B 335, with the SMA ¹²CO (2–1) observations (Yen et al. 2010). The inclination corrected ¹²CO (2–1) compact component associated with B 335 is estimated to have a velocity of 160 km s⁻¹ with a size scale of 1000 AU, and these high-velocity components are roughly elongated along the outflow axis. The ¹²CO (2–1) blueshifted component associated with the L1521F shows similar features in the channel maps and the PV-diagram (showing a relatively high-velocity component compared with wide-opening angle outflow), although the velocity range is much smaller than those observed in B 335. The centrally condensed high-velocity components might show a hint of the earliest evolutionary stage of the high-velocity outflow/jet.

In summary, the low-velocity CO emission is originated to the specially extended emission (Figure 2), while the high-velocity component is originated to the spatially unresolved compact component (Figure 3). Although the extended CO low-velocity emission likely shows the fan-shaped structure (especially at the blueshifted component) as seen in protostellar outflow, their velocity structure is not consistent with the Hubble-like velocity outflow (i.e., parabolic shaped velocity structure in the PV diagram), which is expected in the wide-angle wind model such as observed toward a few Class 0 sources: HH 211, HH 212 and L1448C (Lee et al. 2000 2007a 2007b; Hirano et al. 2010). The high-velocity components may trace the collimated outflow from the protostellar core at the earliest evolutionary stage. Possible interpretations for the velocity structure of the L1521F outflow will be further discussed in Section 4.2.2.

3.5. Outflow Parameters

The outflow properties obtained from the CO data are calculated following the standard method by Cabrit & Bertout (1990). The definition of the outflow parameters are same as the previous studies of VeLLOs (e.g., Pineda et al. 2001; Dunham et al. 2011), so that we can make the comparisons of outflow parameters in following sections. As we discussed in the previous section, two velocity components (e.g., the low-velocity extended component and the higher-velocity compact component) are suggested. In order to separately discuss the low-velocity and higher-velocity components (Section 4.2), the outflow parameters are estimated

according to the following velocity ranges: (i) low-velocity component (LVC; $V_{\text{LSR}}=5.1\text{--}6.6$ km s $^{-1}$; $\Delta V = 1.6$ km s $^{-1}$) and (ii) high-velocity component (HVC; $V_{\text{LSR}} = 2.9\text{--}4.5$ km s $^{-1}$; $\Delta V = 4.2$ km s $^{-1}$) as denoted in Figure 5. Note that the systemic velocity of the source is 6.5 km s $^{-1}$, so our high- and low-velocity definitions are with respect to that velocity, and only refer to the blueshifted emission.

Two methods are usually used to calculate the upper and lower limits to the outflow mass: (i) LTE mass assuming the gas is optically thin, and (ii) LTE mass with an opacity correction. Furthermore, we may miss some emission that has been filtered by the interferometer sampling, therefore, these values are strict lower limits to the mass. In order to calculate the lower limit of the mass, optically thin emission was assumed. Moreover, a significant amount of redshifted emission is probably missed due to the absorption by foreground gas (Section 3.3). Taking account of this, the blueshifted gas was used to estimate outflow parameters.

Measuring the flux with a signal level more than 3σ in each channel⁴, the LTE masses measured in the blue shifted component was estimated to be $3.9\times 10^{-4} M_{\odot}$ and $5.7\times 10^{-5} M_{\odot}$ for LVC and HVC, respectively. Here, the excitation temperature of the CO (2–1) emission was assumed as 20 K (e.g., Hogerheijde et al. 1998; Bourke et al. 2006). Even when a different excitation temperature is adopted between 10–50 K, derived outflow masses change within a factor of 2 (Bourke et al. 2006). Line opacity corrections are also required. The optical depth can be derived as follows;

$$\frac{S_{\nu}({}^{12}\text{CO})}{S_{\nu}({}^{13}\text{CO})} = \frac{[{}^{12}\text{CO}]}{[{}^{13}\text{CO}]} \left(\frac{1 - e^{-\tau}}{\tau} \right) \quad (2)$$

where $[{}^{12}\text{CO}]/[{}^{13}\text{CO}]$ and $S_{\nu}({}^{12}\text{CO})/S_{\nu}({}^{13}\text{CO})$ are the abundance ratio and the intensity ratio between ${}^{12}\text{CO}$ and ${}^{13}\text{CO}$, respectively. Adopting the abundance ratio $[{}^{12}\text{CO}]/[{}^{13}\text{CO}]$ of ≈ 60 (Wilson & Rood 1994), and peak intensity ratio of ≈ 7 as $S_{\nu}({}^{12}\text{CO})/S_{\nu}({}^{13}\text{CO})$, the optical depth of ≈ 9 was estimated⁵. The typical optical depth of ${}^{12}\text{CO}$ is expected to be 2–5 (Levreault 1988). With these opacity corrections, the outflow mass and related physical parameters will be correspondingly greater than our lower limits by similar factors. Assuming that the blueshifted and redshifted components have a similar outflow mass, the lower limit of the outflow mass are estimated to be $M_{\text{CO}}=2\times M_{\text{CO}(\text{blue})}=7.8\times 10^{-4} M_{\odot}$ and

⁴Images after the primary beam correction were used for the flux measurements

⁵Detected ${}^{13}\text{CO}$ (2–1) emission is weak ($\leq 5\sigma$) and the ${}^{13}\text{CO}$ emission mainly traces the ambient gas with the missing flux, the opacity estimation may not be reasonable. Detailed analysis of the ${}^{13}\text{CO}$ will be a future work with better sensitivity.

$M_{\text{CO}}=1.1\times 10^{-4} M_{\odot}$ for the LVC and HVC, respectively. Adopting the optical depth of ~ 9 , the outflow mass for LVC and HVC are estimated to be $7.0\times 10^{-3} M_{\odot}$ and $9.9\times 10^{-4} M_{\odot}$.

The outflow momentum (P_{flow}) and outflow energy (E_{flow}) were estimated as $P_{\text{flow}} = \Sigma M_{\text{flow}}(j) \times |v_j - v_{\text{sys}}|$ and $E_{\text{flow}} = \frac{1}{2} \Sigma M_{\text{flow}}(j) \times |v_j - v_{\text{sys}}|^2$, respectively. Here M_{flow} is the outflow mass in voxel j , v_{sys} is the systemic velocity of 6.5 km s^{-1} , and v_j is the velocity of voxel j . The outflow characteristic velocity v_{flow} is defined as $P_{\text{flow}}/M_{\text{flow}}$. The outflow size, R_{flow} , was measured from the integrated intensity map shown in Figure 2, where the emission signal to noise ratio of more than 3. Measured size was not deconvolved size. The outflow characteristic velocity and the outflow size can be corrected for the inclination angle i with $v_{\text{flow}} = v_{\text{obs}} \times [1/\sin i]$ and $R_{\text{flow}} = R_{\text{obs}} \times [1/\cos i]$, respectively. In this case, projected characteristic outflow velocity and outflow size are defined as v_{obs} and R_{obs} , respectively. The inclination angle of L1521F-IRS (envelope structure) was estimated to be 50° – 70° from the SED and infrared image by Terebey et al. (2009). This corresponds to an outflow inclination angle of between 20° – 40° . For the outflow estimation, the mid value of 30° is assumed. Varying the inclination angle between 20° and 40° changes the outflow size and outflow velocity factor of 1.2 and 1.9, respectively. The dynamical time of the outflow is calculated to be $t_d = R_{\text{flow}}/v_{\text{flow}}$ using the characteristic outflow velocity. Finally, momentum rate (outflow force), mechanical luminosity, and mass loss rate are calculated to be ($F_{\text{obs}} = P/t_d$), ($L_m = M_{\text{CO}} \times v_{\text{flow}}^3/2R$), ($\dot{M}_{\text{out}} = M_{\text{CO}}/t_d$), respectively.

Note that the upper limit and inclination corrected outflow parameters are used in the following subsections. This is because the CO (2–1) emission is most likely optically thick in the molecular outflow (e.g., Leveault 1988 as well as our estimations; See section 3.3.2). Moreover, in order to include the redshifted outflow, which is not detected (most probably due to the self-absorption as discussed in Section 3.3), the outflow parameters described in the following Section are simply multiply factor two of the blueshifted outflow parameters.

4. DISCUSSION

4.1. Origin of the SMA 1.3 mm Continuum Emission

Our SMA observations detected 1.3 mm continuum emission associated with the Spitzer source, L1521F-IRS at an angular resolution of $4.8'' \times 4.4''$ although its peak position is shifted from L1521F-IRS. Recent PdBI observations at a much higher angular resolution by Maury et al. (2010), $0.49'' \times 0.27''$, detected a weak and compact continuum source embedded within the extended continuum source detected with the SMA. In this Section, we will discuss the origin of the dust continuum emission.

Crapsi et al. (2004) fitted the 1.2 mm continuum results obtained from a single-dish telescope with a flat-top core density structure using the semi analytic model of $n(r) = n_0/(1 + (r/r_0)^\alpha)$ (Tafalla et al. 2002) with $n_0 = 10^6 \text{ cm}^{-3}$, $r_0 = 2800 \text{ AU}$, and $\alpha=2$, which is consistent with an isothermal sphere. In order to investigate the origin of the observed SMA 1.3 mm continuum emission on smaller scales, simple power-law models are compared to the data. Specifically, the (i) inside-out collapse model $-\rho(r) \propto r^{-1.5}$ by Shu (1977), and (ii) isothermal sphere model $-\rho(r) \propto r^{-2}$ by Larson (1969) and Penston (1969), are computed and directly compared to the SMA data using the SMA uv-coverage and imaged with the same tapering parameter we used in Figure 1. Here, we adopted the gas temperature of 10 K (e.g., Myers & Benson 1983). We assumed that the parental core has a diameter of 4200 AU and the total flux is 5.8 Jy at 1.3 mm based on 1.2 mm single-dish results by Kauffman et al. (2008). The total and peak fluxes are measured from the simulated image using 2D Gaussian fitting, finding (i) total flux density of $\sim 11 \text{ mJy}$ for the inside-out collapse model, and (ii) total flux density of $\sim 50 \text{ mJy}$ for the isothermal sphere core model. This shows that the the observed flux density, 11 mJy, measured from the two dimensional Gaussian fitting is comparable to or smaller than that expected to arise from inner regions of a molecular envelope, suggesting that the observed emission is unlikely arising from an additional component, such as a disk, in addition to an envelope.

The 1.3 mm continuum emission detected with the PdBI is probably arising from the most inner part of the gas envelope because the PdBI continuum position is coincide with *Spitzer* source position (L1521F-IRS). The positional shift of the peak position between the SMA and PdBI continuum results is not clear because the extended structure detected with the SMA have not been spatially resolved and the visibility amplitude plot does not indicate clear structure.

One possible interpretation to explain the positional shift is the asymmetrical nebula structure originated to the outflow inclination. As we seen in Figure 2(a), the infrared reflection nebula is brighter at west, while less brighter at east. This is likely due to that the western lobe is pointing toward us, and the emission from the eastern lobe is partially absorbed by the foreground dense gas. If similar situation occur in the 1.3 mm continuum emission, the emission peak could be shifted toward the western lobe.

Our SMA observations and the PdBI observations by Maury et al. (2010) have different mass sensitivities and uv-coverage. The 1.3 mm peak flux reported from the PdBI observations, 1 mJy beam^{-1} (with the PdBI beam size of $0''.49 \times 0''.27$), is similar to the noise level of the SMA image, $1.3 \text{ mJy beam}^{-1}$ (with the SMA beam size of $4''.81 \times 4''.43$). This huge beam surface area difference between the PdBI and SMA (factor of ~ 160) suggests that the present SMA observations are not able to detect the compact continuum peak detected

with the PdBI. Furthermore, the PdBI observations cover the baseline ranging from 24 m to 760 m, while our SMA observations cover the base line range of 12 m to 69 m. Even with the simple uv -length range comparison, the SMA observations are at least twice as sensitive to the extended emission compared with PdBI observations, but PdBI observations are more sensitive for resolving the compact structure.

Imaging simulations and observational sensitivity comparisons suggest the 1.3 mm continuum emission detected with the SMA most likely traces the thermal dust emission from the inner envelope rather than emission from circumstellar disk, while the 1.3 mm continuum emission detected with the PdBI as well as *Spitzer* sources trace the warm dust originated from the inner envelope/circumstellar disk.

4.2. Nature of L1521F

The main purpose for studying L1521F is to understand nature of this source as well as the nature of VeLLOs. L1521F (MC 27) was originally noticed as a starless condensation with a high central density of $\sim 10^6 \text{ cm}^{-3}$ (Onishi et al. 1998). Infalling asymmetry spectra observed in the HCO^+ (4–3/3–2) emissions suggest infalling gas motion with the size scale of 2000–3000 AU (Onishi et al. 1999). Molecule depletion observed in CCS and the enhanced deuterium fraction imply the chemically evolved starless core (Shinnaga et al. 2004; Crapsi et al. 2004), which may be about to form a star. The *Spitzer* observations discovered a reflection nebula and a point source associated with L1521F (Bourke et al. 2006). As noted in Terebey et al. (2009) and Saigo et al. (2011), L 1521-IRS is not likely FHSC since the near to mid infrared source (i.e., Spitzer/IRAC bands) was clearly detected. In addition, detection of the 50 AU scale compact continuum source at 1.3 mm may suggest the presence of a circumstellar disk (Maury et al. 2010). Detection of compact high-velocity gas in the CO (2–1) line also supports the presence of a molecular outflow. These observational facts suggest that L1521F-IRS is already in the protostellar phase (i.e., after second collapse phase) with the very low internal luminosity of $< 0.07 L_{\odot}$ (Bourke et al. 2006; Dunham et al. 2008; Terebey et al. 2009).

4.2.1. Evolutionary Status

Here, we assume a standard accretion rate at the main accretion phase, $1.6 \times 10^{-6} M_{\odot} \text{ yr}^{-1}$, derived from c_s/G^3 (e.g., Shu et al. 1977) at $T \approx 10 \text{ K}$ (e.g., Myers & Benson 1983). Here, c_s is the sound speed and G is the gravitational constant. This accretion rate is similar to

those directly measured in low-mass star forming regions (e.g., Ohashi et al. 1997; Saito et al. 2001). The current stellar mass can be estimated from $L_{\text{acc}} = GM_*\dot{M}_{\text{acc}}/R_*$. Considering the internal luminosity of L1521F of 0.034–0.07 L_{\odot} (Bourke et al. 2006; Tereby et al. 2009) is mainly due to the accretion luminosity $L_{\text{acc}}(\approx L_{\text{int}})$, and assuming the stellar radius is $R_* \sim 3R_{\odot}$ (Palla 2002), and the standard accretion rate, the stellar mass is estimated to be 0.002–0.004 M_{\odot} , or 2–4 M_J .

The estimated mass of the central protostar, assuming the standard accretion rate is a factor of 2.5–5 smaller than the minimum mass of FHSC or a second core, 0.01 M_{\odot} , derived from the theoretical calculations (e.g., Masunaga & Inutsuka 1998; Bete 2011; Machida et al. 2011). In order for the current stellar mass to be 0.01 M_{\odot} at the observed L_{int} , the mass accretion rate should be at least four times smaller, i.e., $\dot{M}_{\text{acc}} \sim 4 \times 10^{-7}$. Such a small mass accretion rate is not expected in standard star formation theories, whereas it can be expected in a scenario of non-steady accretion (e.g., Hartmann & Kenyon 1996; Vorobyov & Basu 2005, 2006; Machida et al. 2011). Recent Magnetohydrodynamic (MHD) simulations by Machida et al. (2011) suggest that the mass accretion rate suddenly decreases to $10^{-5} M_{\odot} \text{ yr}^{-1}$ right after a central protostar is formed, and the accretion rate gradually decreases afterward. We note that such a small mass accretion rate would be inconsistent with a relatively larger mass outflow rate of L1521F-IRS because $\dot{M}_{\text{w}} \approx (0.1-0.5)\dot{M}_{\text{acc}}$ (e.g., Hartigan et al. 1995), where \dot{M}_{w} is the mass loss rate. When we assume that 10% of the accreting material is ejected as an outflow, the mass accretion rate is estimated to be $\dot{M}_{\text{acc}} = 1.5 \times 10^{-6} - 9.7 \times 10^{-5} M_{\odot} \text{ yr}^{-1}$. Here, the mass accretion rate were calculated based on the mass outflow rate listed in Table 2 as $\dot{M}_{\text{acc}} = \dot{M}_{\text{w}}/0.1 = 2 \times (\dot{M}_{\text{out(LVC)}} + \dot{M}_{\text{out(HVC)}})/0.1$. This mass outflow rate, however, is an outflow rate averaged over the period of the dynamical time scale of the outflow, meaning that the mass infall rate estimated from the mass outflow rate based on $\dot{M}_{\text{w}} \approx 0.1\dot{M}_{\text{acc}}$ is also an averaged value over the dynamical time scale. When non-steady accretion is considered, the current accretion rate can be smaller than the averaged mass accretion rate. Dunham et al. (2011) made comparisons of outflow parameters measured toward VeLLOs that have been observed at high angular resolution, which includes candidate FHSCs, very young protostellar cores, and candidate proto-brown dwarfs. The mass outflow rate toward them, $\dot{M}_{\text{out}} = M_{\text{flow}}/\tau_d$, falls in the range $6.0 \times 10^{-9} - 1.1 \times 10^{-6} M_{\odot} \text{ yr}^{-1}$. Estimated outflow rate toward L1521F is comparable or slightly higher than those observed by Dunham et al. (2011).

As discussed above, the expected time averaged mass accretion rate suggests that half of the VeLLOs reported by Dunham et al. (2011), i.e., L1448-IRAS 2E, CB17 MMS, L1148-IRS, and L673-7-IRS, have comparable or larger mass accretion rates compared to those expected in the standard low-mass star formation scenario. This suggests that central stellar mass larger than 0.01 M_{\odot} should already be present, in the case of steady accretion. Time variable

mass accretion processes (i.e., lower mass accretion rate at present), which is also suggested for L1521F, could be responsible for the observed low internal luminosities for some VeLLOs.

4.2.2. *Outflow Morphology and Velocity*

Three-dimensional MHD simulations have been performed on molecular outflows driven by FHSCs and second cores (i.e., protostars; Machida et al. 2008). These simulations predict the presence of a low-velocity flow (5 km s^{-1}) with a wide opening angle, driven from FHSC ($n_c > 10^{12} \text{ cm}^{-3}$), while high velocity flows (30 km s^{-1}) with good collimation, are expected when the central protostar (2nd core; $n_c > 10^{21} \text{ cm}^{-3}$) is formed. Our CO (2–1) outflow observations spatially resolved the less collimated morphology in the low-velocity component of the L1521F outflow ($v_{\text{flow}} = 1.5 \text{ km s}^{-1}$), while the high-velocity outflow ($v_{\text{flow}} = 4.0 \text{ km s}^{-1}$) is extremely compact and associated only with the central region around L 1521-IRS. An interesting characteristic of the extended low-velocity outflow is that it does not follow a Hubble-like velocity structure, which is predicted by the wind-driven model as discussed in Section 3.3.1. These results suggest that the nature of the low-velocity component detected from L1521F-IRS may not be typical of outflows/jets associated with the Class 0/I sources. However, it could be related to the outflow driven from FHSC since they are expected to be of very low-velocity and less collimated, as shown by MHD simulations (Machida et al. 2008).

In reality the outflow from FHSC may have more variety than the less collimated morphology predicted by simulations (Machida et al. 2006; 2008). A very recent smoothed particle magnetohydrodynamics (SPMHD) simulations by Price et al. (2012) demonstrated that collimated jets (opening angles $\leq 10^\circ$) may be present during the collapse of molecular cloud cores to form FHSCs in low-mass star formation. Collimated molecular outflow have been observed from candidate FHSCs such as L1448 IRAS 2E (Chen et al. 2010) and Per-Bolo 58 (Enoch et al. 2010; Dunham et al. 2011).

The detected high-velocity CO (2-1) emission likely traces a collimated molecular outflow, although we have not completely spatially resolved the structure. The measured characteristic outflow velocity after the inclination correction was estimated to be 4.0 km s^{-1} (or the maximum outflow velocity of 7.2 km s^{-1}). This velocity is roughly consistent with the velocity expected of collimated jets originating from FHSCs, $2\text{--}7 \text{ km s}^{-1}$ (Price et al. 2012). However, in L1521F the compact CO (2–1) emission is unlikely to originate from a FHSC, as it is associated with the protostar.

The dynamical time scale of the low- and high-velocity components associated with

L1521F are estimated to be 3800 yr and 1100 yr, respectively. If we assume that the times for the low- and high-velocity outflows reflect the age of first core and second core, respectively, then the age of the second core should also be about 1100 yr. Further, about 2700 yr after the first core was formed, the second collapse occurred. The estimated life time of FHSC is roughly consistent with those estimated from MHD simulations (Machida et al. 2011). Moreover, the estimated mass of the second core is approximately $0.01 M_{\odot}$ about 1000 yrs after the second collapse. This is also consistent with the mass of L1521F-IRS estimated from the internal luminosity in the case of non-steady accretion.

Observations with improved angular resolution and better sensitivity are needed for more detailed comparisons with MHD simulations, and to study the nature of the extended outflow. This will be an important study using ALMA.

4.2.3. Comparisons of Outflow Characteristics

Figure 6 compares the outflow parameters of L1521F (this work) with previously studied outflows associated with low- to high-mass star forming regions (Wu et al. 2004), and outflows associated with VeLLOs (referred from Table 4 in Dunham et al. 2011). The measured outflow mass, size, and outflow force of VeLLOs including L1521F (as well as all the other parameters listed in Table 2) show a small range of values compared to outflows from low to high-mass star forming regions, and are located at the lower end of the range of values seen in all outflows. On the other hand, the derived L1521F outflow parameters share similar characteristics with outflow parameters derived from other VeLLOs as summarized in Dunham et al. (2011).

Outflow masses and sizes are integrated values over the outflow evolution. As clearly seen in Figure 6 (a) and (b), the outflow mass and size reported for VeLLOs including L1521F show orders of magnitude smaller values compared with those of the main population of the previously studied outflows. This may suggest that the outflows associated with VeLLOs are not well developed yet. The dynamical time scale of the outflow could also support this argument: the outflow dynamical time scales derived in VeLLOs are 700 to 61000 yrs, while those derived from previous outflow studies summarized in Wu et al. (2004) ranges 2.0×10^3 – 5.0×10^5 yrs. Note that the outflow dynamical time scale can only tell us lower limits to the real outflow age. Especially if the source become distant, the size underestimation effect become more significant due to the sensitivity limit. However, considering with the distance effect, we still see that the dynamical time scales associated with non-VeLLOs are orders of magnitude shorter in average compared to those in more massive outflows. This clearly implies outflow character differences between them, and the results imply that L 1521F as

well as some of VeLLOs are probably in the earliest evolutionary stage of the protostellar phase ($<10^4$ yr, which is younger than Class 0). Alternatively, it could be that emission from these outflows is hard to detect at larger distances from their driving sources, as the emission is often faint, and may be below the sensitivity limits of current observations.

The dashed square in Figure 6(b) and (c) shows the area where outflows associated with embedded sources in the Taurus star forming region are located (Hogerheijde et al. 1998). L1521F has the lowest bolometric luminosity (i.e., internal luminosity) and the smallest outflow size among the Taurus protostellar candidates. Nevertheless, the estimated outflow parameters such as outflow mass and force, as well as outflow momentum, energy, and mechanical force are comparable to the previously studied low-mass outflow cases. For example, the outflow force derived in embedded protostars in Taurus is $1.9 \times 10^{-7} - 2.2 \times 10^{-3} M_{\odot} \text{ km s}^{-1} \text{ yr}^{-1}$ (e.g., Hogerheijde et al. 1998), while the value for the L1521F outflow is $7.4 \times 10^{-7} - 6.6 \times 10^{-6} M_{\odot} \text{ km s}^{-1} \text{ yr}^{-1}$ (within the dashed square in Figure 6(c)). The outflow parameters reflecting outflow activity such as the outflow force are comparable to some outflows in Taurus. A possible explanation is that L 1521F could be a low-mass protostar similar to other protostars in Taurus. The averaged outflow force (as well as the averaged mass outflow rate and outflow energy) is larger than other outflows in Taurus, while the relatively smaller outflow size (as well as short outflow dynamical time scale) suggest that the L1521F-IRS is in an earlier evolutionary phase than other embedded sources in Taurus.

In summary, the L1521F outflow is one of the smallest in size and youngest in dynamical time among nearby low-mass protostellar cores as same as other VeLLOs, suggesting that L1521F-IRS is in a very early evolutionary phase ($<10^4$ yr). The estimated outflow force, energy, and mass loss rate suggests that the time averaged star formation activity of L1521F-IRS may be similar to other low-mass protostars in Taurus. The extremely smaller internal luminosity of L1521F-IRS might suggest that the mass accretion rate at present is much smaller than the time-averaged value.

5. SUMMARY AND FUTURE PROSPECTS

We have performed CO(2–1) and 1.3 mm continuum observations toward the very low-luminosity object, L1521F-IRS, with the SMA. The main results are summarized as follows:

- We have spatially resolved a molecular outflow associated with L1521F-IRS in CO (2–1) emission for the first time. The blueshifted and redshifted lobes are aligned along the east and west side of L1521F-IRS with a lobe size of ≈ 1000 AU. The estimated outflow mass, the maximum outflow velocity, and the outflow force are $(9.0-80) \times 10^{-4} M_{\odot}$, 7.2

km s⁻¹, and $(7.4-66)\times 10^{-7} M_{\odot} \text{ km s}^{-1} \text{ yr}^{-1}$, respectively.

- The estimated outflow size, mass, and energy are located at the lower end of parameters derived from previously studied outflows associated with low- to high-mass star forming regions, but share similar characteristics to outflows associated with VeLLOs. The CO emission suggests a low-velocity less collimated component (1.5 km s⁻¹/1200 AU) and a high-velocity compact component (4.0 km s⁻²/920 AU). These velocity structures are not consistent with those expected in the jet driven or wind driven outflows, maybe suggesting the presence of the outflow remnant from the FHSC as well as the undeveloped outflow from the protostar.
- The previous detection of an infrared source and compact dust continuum emission suggests the presence of the protostar. Its low bolometric luminosity ($\approx 0.05 L_{\odot}$) and small outflow lobe size, among the smallest of all previously studied outflows, suggest that L1521F-IRS is at least one order of magnitude younger ($< 10^4$ yr) than Class 0 protostars and contains (at present) a substellar object at the center. A comparison between mass outflow rate and minimum requirement for the theoretically predicted initial stellar/core suggests a mass, non-steady accretion model could explain the observational results without contradiction. i.e., the current accretion rate can be smaller than the averaged mass accretion rate.
- Our 1.3 mm continuum observations with the SMA have detected an extended thermal dust component with a mass of 0.047–0.084 M_{\odot} . Our imaging simulations suggest that this emission originates from the inner envelope rather than from a circumstellar disk.

We acknowledge the staff at the Submillimeter Array for assistance with operations. The SMT is operated by the Arizona Radio Observatory (ARO), steward Observatory, University of Arizona. S. T. acknowledges S.-W. Yen for helping the SMT ¹²CO (2–1) data inspection, and M. Machida and N. Hirano for fruitful scientific comments. S. T. is financially supported by a postdoctoral fellowship at the Institute of Astronomy and Astrophysics, Academia Sinica, Taiwan.

REFERENCES

- Bate, M. R. 1998, *ApJ*, 508, L95
- Bate, M. R. 2010, *MNRAS*, 404, L79
- Bate, M. R. 2011, *MNRAS*, 417, 2036
- Belloche, A., André, P., Despois, D., & Blinder, S. 2002, *A&A*, 393, 927
- Belloche, A., Parise, B., van der Tak, F. F. S., et al. 2006, *A&A*, 454, L51
- Bourke, T. L., Crapsi, A., Myers, P. C., Evans, N. J., II, Wilner, D. J., Huard, T. L., Jørgensen, J. K., & Young, C. H. 2005, *ApJ*, 633, L129
- Bourke, T. L., et al. 2006, *ApJ*, 649, L37
- Cabrit, S., & Bertout, C. 1990, *ApJ*, 348, 530
- Chen, X., Arce, H. G., Zhang, Q., Bourke, T. L., Launhardt, R., Schmalzl, M., & Henning, T. 2010, *ApJ*, 715, 1344
- Crapsi, A., Caselli, P., Walmsley, C. M., Tafalla, M., Lee, C. W., Bourke, T. L., & Myers, P. C. 2004, *A&A*, 420, 957
- Crapsi, A., et al. 2005, *A&A*, 439, 1023
- Dunham, M. M., Crapsi, A., Evans, N. J., II, Bourke, T. L., Huard, T. L., Myers, P. C., & Kauffmann, J. 2008, *ApJS*, 179, 249
- Dunham, M. M., Evans, N. J., Bourke, T. L., et al. 2010, *ApJ*, 721, 995
- Dunham, M. M., Chen, X., Arce, H. G., et al. 2011, *ApJ*, 742, 1
- Enoch, M. L., Lee, J.-E., Harvey, P., Dunham, M. M., & Schnee, S. 2010, *ApJ*, 722, L33
- Hartigan, P., Edwards, S., & Ghandour, L. 1995, *ApJ*, 452, 736
- Hartmann, L., & Kenyon, S. J. 1996, *ARA&A*, 34, 207
- Hirano, N., Ho, P. P. T., Liu, S.-Y., et al. 2010, *ApJ*, 717, 58
- Ho, P. T. P., Moran, J. M., & Lo, K. Y. 2004, *ApJ*, 616, L1
- Hogerheijde, M. R., van Dishoeck, E. F., Blake, G. A., & van Langevelde, H. J. 1998, *ApJ*, 502, 315

- Kauffmann, J., Bertoldi, F., Bourke, T. L., Evans, N. J., II, & Lee, C. W. 2008, *A&A*, 487, 993
- Kauffmann, J., Bertoldi, F., Bourke, T. L., et al. 2011, *MNRAS*, 416, 2341
- Larson, R. B. 1969, *MNRAS*, 145, 271
- Lee, C.-F., Mundy, L. G., Reipurth, B., Ostriker, E. C., & Stone, J. M. 2000, *ApJ*, 542, 925
- Lee, C.-F., Ho, P. T. P., Palau, A., Hirano, N., Bourke, T. L., Shang, H., & Zhang, Q. 2007, *ApJ*, 670, 1188
- Lee, C.-F., Ho, P. T. P., Hirano, N., Beuther, H., Bourke, T. L., Shang, H., & Zhang, Q. 2007, *ApJ*, 659, 499
- Levreault, R. M. 1988, *ApJS*, 67, 283
- Luhman, K. L., Mamajek, E. E., Allen, P. R., & Cruz, K. L. 2009, *ApJ*, 703, 399
- Machida, M. N., Inutsuka, S.-i., & Matsumoto, T. 2006, *ApJ*, 647, L151
- Machida, M. N., Inutsuka, S.-i., & Matsumoto, T. 2008, *ApJ*, 676, 1088
- Machida, M. N., Inutsuka, S.-i., & Matsumoto, T. 2011, *ApJ*, 729, 42
- Masunaga, H., Miyama, S. M., & Inutsuka, S.-I. 1998, *ApJ*, 495, 346
- Masunaga, H., & Inutsuka, S.-i. 2000, *ApJ*, 531, 350
- Maury, A. J., et al. 2010, *A&A*, 512, A40
- Mizuno, A., Onishi, T., Hayashi, M., Ohashi, N., Sunada, K., Hasegawa, T., & Fukui, Y. 1994, *Nature*, 368, 719
- Myers, P. C., & Benson, P. J. 1983, *ApJ*, 266, 309
- Ohashi, N., Hayashi, M., Ho, P. T. P., & Momose, M. 1997, *ApJ*, 475, 211
- Onishi, T., Mizuno, A., Kawamura, A., Ogawa, H., & Fukui, Y. 1998, *ApJ*, 502, 296
- Onishi, T., Mizuno, A., & Fukui, Y. 1999, *PASJ*, 51, 257
- Ohashi, N., Lee, S. W., Wilner, D. J., & Hayashi, M. 1999, *ApJ*, 518, L41
- Palla, F. 2002, *Physics of Star Formation in Galaxies*, 9

- Penston, M. V. 1969, MNRAS, 144, 425
- Pineda, J. E., Goodman, A. A., Arce, H. G., et al. 2010, ApJ, 712, L116
- Price, D. J., Tricco, T. S., & Bate, M. R. 2012, MNRAS, 423, L45
- Ossenkopf, V., & Henning, T. 1994, A&A, 291, 943
- Saigo, K., Tomisaka, K., & Matsumoto, T. 2008, ApJ, 674, 997
- Saigo, K., & Tomisaka, K. 2011, ApJ, 728, 78
- Saito, M., Kawabe, R., Kitamura, Y., & Sunada, K. 2001, ApJ, 547, 840
- Schönke, J., & Tscharnuter, W. M. 2011, A&A, 526, A139
- Scoville, N. Z., Carlstrom, J. E., Chandler, C. J., Phillips, J. A., Scott, S. L., Tilanus, R. P. J., & Wang, Z. 1993, PASP, 105, 1482
- Shinnaga, H., Ohashi, N., Lee, S.-W., & Moriarty-Schieven, G. H. 2004, ApJ, 601, 962
- Shinnaga, H., Phillips, T. G., Furuya, R. S., & Kitamura, Y. 2009, ApJ, 706, L226
- Shu, F. H. 1977, ApJ, 214, 488
- Stahler, S. W., Shu, F. H., & Taam, R. E. 1980, ApJ, 242, 226
- Tafalla, M., Mardones, D., Myers, P. C., Caselli, P., Bachiller, R., & Benson, P. J. 1998, ApJ, 504, 900
- Tafalla, M., Myers, P. C., Caselli, P., Walmsley, C. M., & Comito, C. 2002, ApJ, 569, 815
- Terebey, S., et al. 2009, ApJ, 696, 1918
- Vorobyov, E. I., & Basu, S. 2005, ApJ, 633, L137
- Vorobyov, E. I., & Basu, S. 2006, ApJ, 650, 956
- Wilner, D. J., & Welch, W. J. 1994, ApJ, 427, 898
- Wilson, T. L., & Rood, R. 1994, ARA&A, 32, 191
- Wu, Y., Wei, Y., Zhao, M., et al. 2004, A&A, 426, 503
- Yen, H.-W., Takakuwa, S., & Ohashi, N. 2010, ApJ, 710, 1786
- Young, E. T., et al. 2004, ApJS, 154, 428

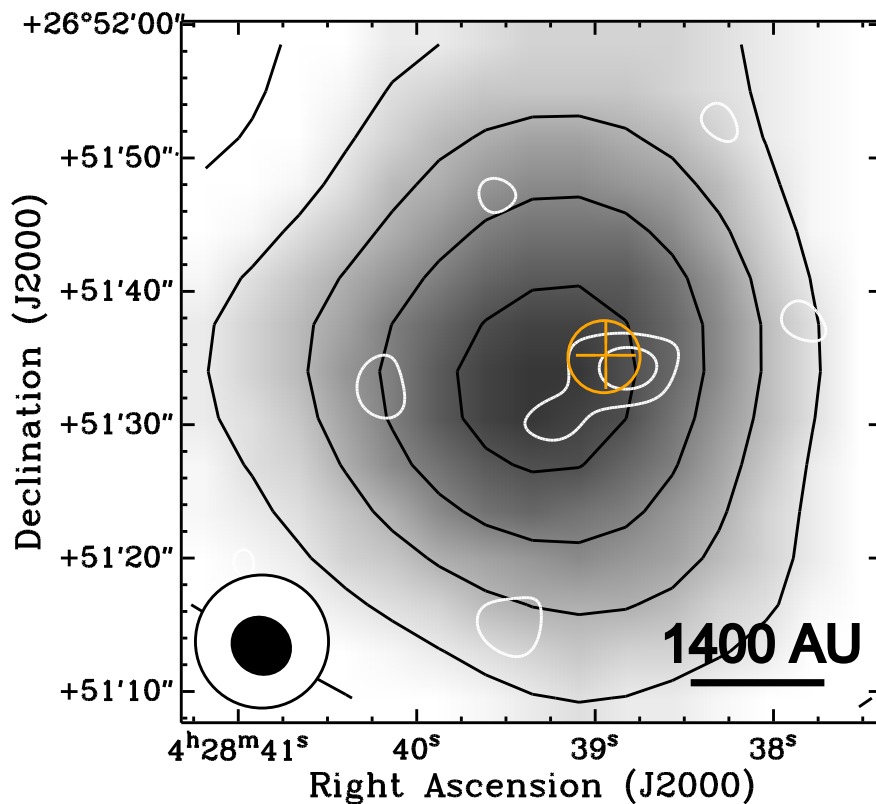


Fig. 1.— The 1.3 mm continuum image from SMA observations in white contours superposed on the 1.2 mm continuum image taken with the IRAM 30m/MAMBO-2 by Kauffmann et al. (2008) in grey scale and black contours. The contour levels of the SMA continuum emission start at $\pm 2\sigma$ with a interval of 2σ ($1\sigma = 1.3 \text{ mJy beam}^{-1}$). The contour levels of the 1.2 mm image taken with the IRAM 30m/MAMBO-2 are 29.5, 37.5, 45.5, 53.5, and 61.5 mJy beam^{-1} , respectively. The cross and circle show the positions of the PdBI 1.3 mm and Spitzer sources (L1521F-IRS), referred from Maury et al. (2010) and Bourke et al. (2006), respectively. Open and filled ellipses in the bottom left corner shows the beam sizes of IRAM 30m/MAMBO-2 and SMA, respectively.

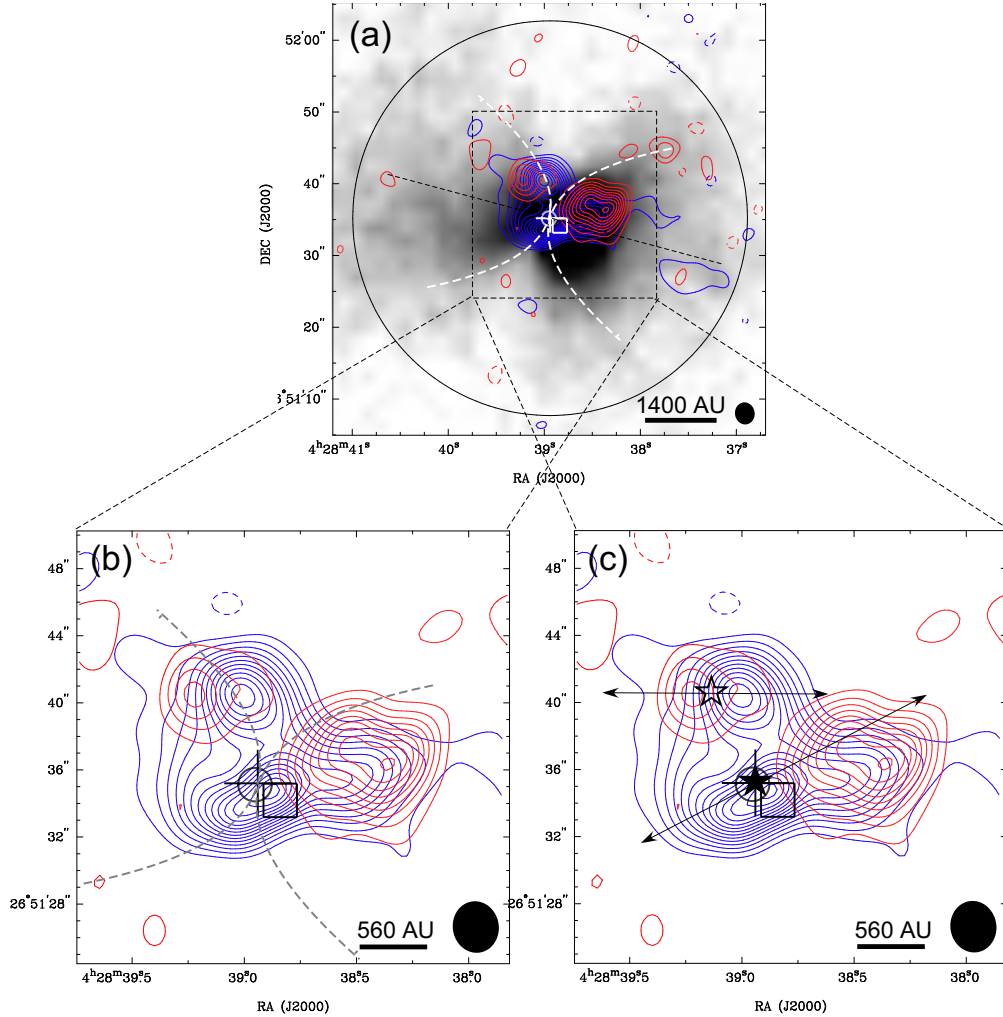


Fig. 2.— (a) Blueshifted and redshifted velocity components of the CO (2–1) emission in contours taken with the SMA superposed on the 4.5 μm image obtained with *Spitzer*/IRAC (Bourke et al. 2006). The large circle represent the FWHM size of the SMA primary beam, while the filled ellipse at bottom right shows the synthesized beam size. (b) Zoomed in image of the CO (2–1) blueshifted and redshifted components. The velocity ranges of the blueshifted and redshifted emission are $V_{\text{LSR}}=2.9\text{--}6.1\text{ km s}^{-1}$ and $V_{\text{LSR}}=8.2\text{--}10.4\text{ km s}^{-1}$, respectively. The contour lines start at $\pm 3\sigma$ levels, with intervals of 3σ ($1\sigma_{\text{(blue)}} = 0.35\text{ Jy beam}^{-1}\text{ km s}^{-1}$; $1\sigma_{\text{(red)}} = 0.24\text{ Jy beam}^{-1}\text{ km s}^{-1}$). Negative contours are represented by dashed lines. The peak positions of the PdBI 1.3 mm continuum source (Maury et al. 2010), infrared (IRAC) source (Bourke et al. 2006), and SMA 1.3 mm continuum source (this work) are denoted in the cross, open circle, and square, respectively. The green and grey dotted lines show the guide lines for the parabolic shaped molecular outflow originated from the wide angle wind model as discussed in Section 3.4. (c) The schematic picture of possible multiple outflows. Open and filled stars present the position of L1521F-IRS and L1521F-NE (if exists).

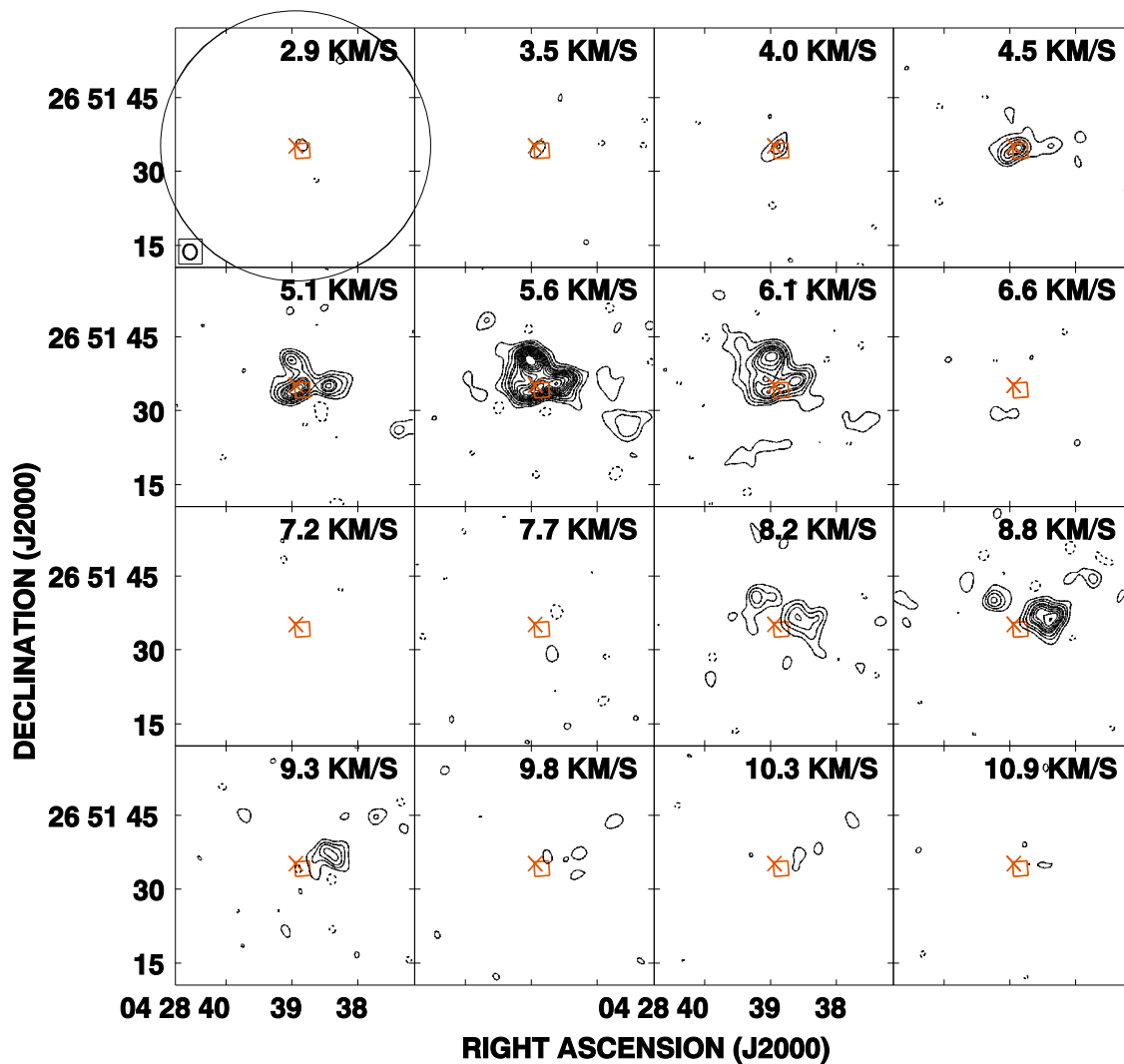


Fig. 3.— Velocity channel maps of the ^{12}CO (2–1) emission taken with the SMA. The central LSR velocity in units of km s^{-1} is noted at the upper right corner of each panel. The contour levels start at 3σ levels, with intervals of 3σ ($1\sigma=0.13 \text{ Jy beam}^{-1}$). Crosses and square in the maps show the peak positions of the PdBI 1.3 mm (as well as infrared source detected with *Spitzer/IRAC*) and SMA 1.3 mm source, respectively. The large circle in the upper-left panel shows the SMA primary beam size, while the open ellipse in the bottom left corner shows the SMA synthesized beam, respectively. Negative contours are shown as black dashed lines.

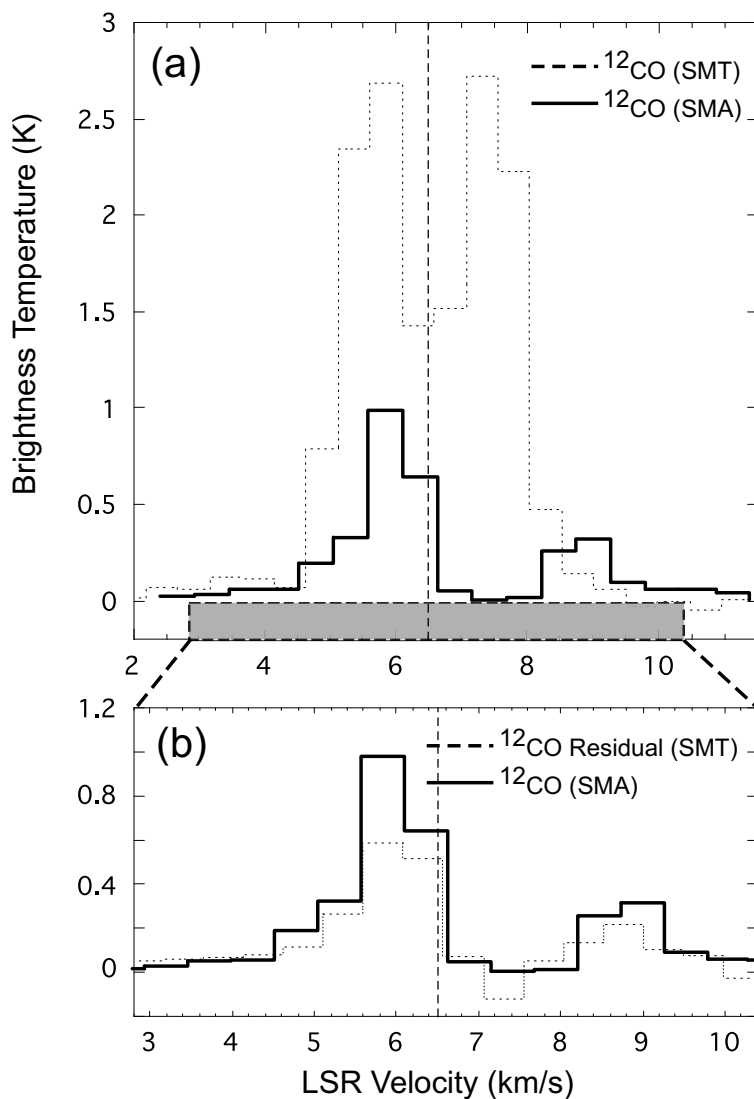


Fig. 4.— (a) Comparison of the SMT and SMA ^{12}CO (2-1) spectra at the position of L1521F-IRS. The SMA data are convolved to the SMT $32''$ beam, (b) ^{12}CO (2-1) spectrum taken with the SMA compared with the ^{12}CO residual spectrum. The residual spectrum is derived by subtracting from the central spectrum the mean spectrum from positions $30''$ away. Dashed lines show the system velocity of L1521F of 6.5 km s^{-1} .

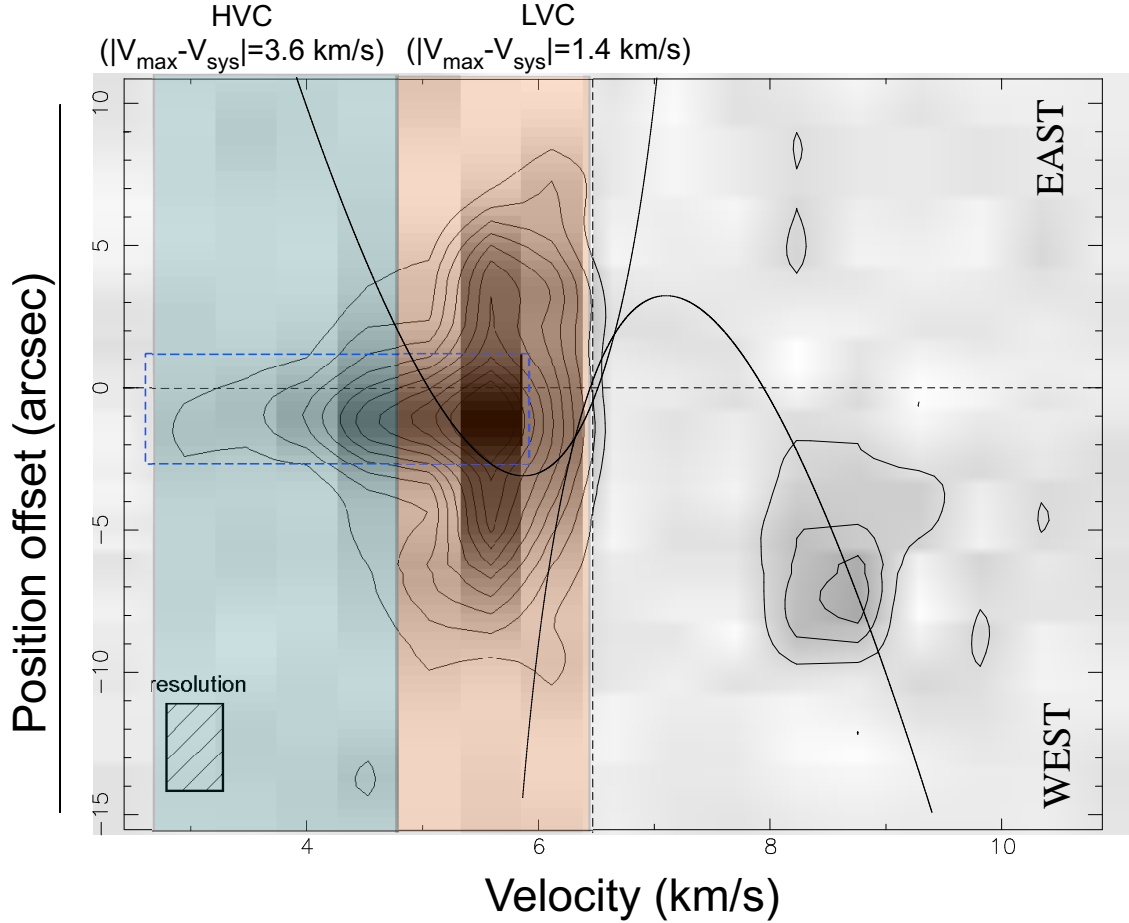


Fig. 5.— Position-velocity diagram of ^{12}CO (2–1) cut along the outflow axis (P. A. = 75°). The contour level starts at 3σ with intervals of 3σ ($1\sigma = 0.13 \text{ Jy beam}^{-1} \text{ km s}^{-1}$). Dashed lines in the diagram show the systemic velocity (6.5 km s^{-1}) and the protostar position. The solid black curve is the wide-angle wind model curve produced by setting $i = 60^\circ$, $C = 0.022 \text{ arcsec}^{-1}$, $v_0 = 0.05 \text{ km s}^{-1}$. The filled square at the bottom left corner shows the spatial and velocity resolution. The red box and blue box show the velocity ranges of the low-velocity component ($|v_{\max} - v_{\text{sys}}| = 1.4 \text{ km s}^{-1}$) and the high-velocity component ($|v_{\max} - v_{\text{sys}}| = 3.6 \text{ km s}^{-1}$), respectively.

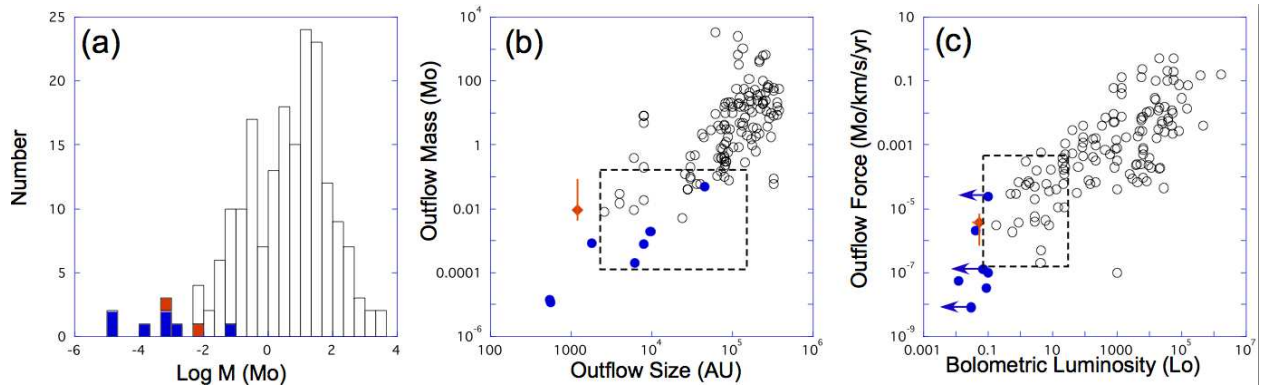


Fig. 6.— (a) Outflow mass histogram. The lower limit (optically thin condition) and upper limit ($\tau=9$) estimated in L1521F was denoted by orange color, (b) outflow mass plotted as a function of outflow size, and (c) outflow force plotted as a function of bolometric luminosity. Orange symbols/histogram denote the outflow from L1521F (this work). Open symbols/histograms show parameters reported in previous low to high-mass outflow studies by Wu et al. (2004), while blue symbols/histograms show parameters reported for outflows associated with VeLLOs by Dunham et al. (2011). The values presented for 129 outflows extracted from Wu et al. (2004) are obtained from online tables that list outflow size, mass, force, and bolometric luminosity of the central source. The outflow parameters range derived in Taurus by Hogerheide et al. (1998) was denoted as dashed squares in figure (b) and (c).

Table 1. SMA Observational Parameters

Parameter	Value
Observing Date (UT)	Jan. 3, 2007
Reference position (J2000.0)	$\alpha=4^h 28^m 38.95^s$, $\delta=+26^\circ 51' 35.10''$
Configurations	compact
Primary beam HPBW [arcsec]	55
Synthesized Beam HPBW of 1.3 mm continuum emission [arcsec]	4.8×4.4 (53)
Synthesized Beam HPBW of CO (2–1) emission [arcsec]	3.1×2.7 (9.1)
Equivalent frequency [GHz]	214.534
Bandwidth [GHz]	4.0
Velocity resolution of CO (2–1) emission [km s ^{−1}]	0.53
Projected base line range of continuum / CO (2–1) [kλ]	9.1–53 / 9.5–53
Maximum detectable structure of continuum/CO (2–1) [arcsec]	18 / 17
Gain calibrators (flux of Gain calibrators in Jy)	3C 111 (3.0 Jy)
Bandpass calibrator	3C 279
Primary flux calibrators	Uranus
RMS noise level of continuum emission [mJy beam ^{−1}]	1.3
RMS noise level of CO (2–1) emission [Jy beam ^{−1}]	0.13

^aOur observations were insensitive to more extended emission than this size-scale structure at the 10% level (Wilner & Welch 1994).

Table 2. Outflow Parameters Measured from the Blueshifted Emission ^d

Parameters	LVC		HVC	
	Uncorrected ^a	Corrected ^b	Uncorrected ^a	Corrected ^b
Mass (M_\odot) ^c	(3.9–35)e-04	(3.9–35)e-04	(5.7–51)e-05	(5.7–51)e-05
Characteristic velocity (km s ^{−1})	0.8	1.5	2.1	4.0
Size (AU)	1000	1200	800	920
Dynamical Time (yr)	6200	3800	1800	1100
Momentum (M_\odot km s ^{−1})	(3.0–27)e-04	(5.9–53)e-04	(1.2–11)e-04	(2.3–21)e-04
Kinetic energy (M_\odot km ² s ^{−2})	(1.3–12)e-04	(5.3–48)e-04	(1.2–11)e-04	(4.8–43)e-04
Outflow force (M_\odot km s ^{−1} yr ^{−1})	(4.9–44)e-08	(1.6–14)e-07	(6.6–61)e-08	(2.1–19)e-07
Mechanical luminosity (L_\odot)	(3.0–28)e-06	(1.9–17)e-05	(1.1–10)e-05	(6.9–62)e-05
Mass Loss rate (M_\odot yr ^{−1})	(6.3–57)e-08	(1.0–9.2)e-07	(3.1–28)e-08	(5.2–47)e-08

^aThe inclination angle is not corrected

^bThe inclination angle is corrected. The outflow inclination angle was assumed as 30°.

^cThe outflow mass is estimated using the blueshifted emission assuming with the optically thin gas and the LTE condition.

^dThe lower limit values are derived with optically thin conditions, while the upper limit values are derived with the opacity of ~ 9 . After Section 4.2, the upper limit values are used for the outflow discussions.